Double K-shell vacancy production in the electron capture decay of ^{125}I

M.M. Hindi and R.L. Kozub
Physics Department, Tennessee Technological University, Cookeville, Tennessee 38505
(Received 4 November 1991)

We have measured the probability of double K-shell vacancy production in the electron capture decay of ^{125}I to the 35-keV level of ^{125}Te. The probability was deduced from the number of triple coincidences between the Te hypersatellite and satellite x rays produced in filling the double vacancy, and the subsequent normal x ray accompanying the K internal conversion of the 35-keV level. The probability of double K-shell vacancy production per K-shell electron capture (P_{KK}) was found to be $(1.35 \pm 0.15) \times 10^{-5}$.

PACS number(s): 23.40.-s, 23.90.+w, 27.60.+j, 32.80.Hd

I. INTRODUCTION

When a nucleus decays by capturing an electron from the K shell, the sudden change of the nuclear charge from Ze to $(Z-1)e$ and the concomitant disappearance of the electron can cause the remaining electron in the K shell to be excited to unoccupied levels (shakeup, SU) or to continuum states (shakeoff, SO), thus leaving a double vacancy in the shell. The probability P_{KK} of double K-shell vacancy production per K-electron capture has been measured for 14 isotopes. The results of these measurements have been summarized in Ref. [1]. The measured values decrease from $\sim 10^{-4}$ at $Z = 18$ to $\sim 10^{-6}$ at $Z = 83$. The decrease appears to be monotonic, except for decays with low Q value (^{109}Cd, ^{139}Ce, ^{181}W), which have P_{KK}'s that are lower than the general trend.

The various theoretical approaches to calculating P_{KK} have been summarized recently by Campbell, Maxwell, and Teesdale [2]. The two most sophisticated theoretical approaches are the semirelativistic propagator (SRP) method of Intemann [3], and the self-consistent-field (SCF) method of Suzuki and Law (SL) [4]. These two theories bracket most of the measured values, with the SCF theory being on the high side and the SRP theory on the low side. For decays with low Q value, however, both theories predict P_{KK}'s that are lower than the measured values, suggesting that the calculations fall to zero (with decreasing Q value) faster than the experimental data. This observation, however, is based on comparison with the measured values of only three isotopes (^{109}Cd, ^{139}Ce, and ^{181}W), all of which have rather large errors on their measured values (36%, 80%, and 25%, respectively). Thus, to extend the base of experimental systematics, and to help in testing the validity of this observation, we sought to measure the P_{KK} of ^{125}I, which also has a low Q value for electron capture (EC) decay.

Experiments to measure P_{KK} usually record coincidences between the hypersatellite ($K\alpha^H$) and satellite ($K\alpha^S$) x rays produced in the transitions $1s^{-2} \rightarrow 1s^{-1}2p^{-1}$ and $1s^{-1}2p^{-1} \rightarrow 2p^{-2}$, respectively. For ^{125}I (decay scheme shown in Fig. 1), however, $K\alpha^S \otimes K\alpha^H$ coincidences would be overwhelmed by the tail of the $K\alpha^N \otimes K\alpha^N$ coincidences between the normal x ray produced in EC and the subsequent normal x ray accompanying the K-shell internal conversion (IC) of the 35-keV level in ^{125}Te, as this level decays mostly by IC ($e/\gamma = 14.02$ [5]). Thus, to eliminate the interference of these double coincidences, we measured triple coincidences between the satellite and hypersatellite x rays produced in filling the double vacancy, and the subsequent normal x ray accompanying the K-shell IC of the 35-keV level. Since the transition energy of 35 keV is too low to doubly ionize the K shell ($1s$ binding energy = 31.814 keV [6]), double vacancies in the K shell can only be created during the EC decay of ^{125}I, and cannot be initiated by the subsequent IC of the 35-keV level in ^{125}Te.

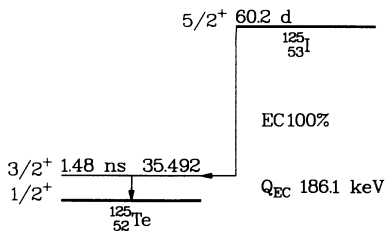

FIG. 1. Decay scheme of ^{125}I. The level energy is in keV.

II. EXPERIMENTAL PROCEDURE

Our experimental technique consisted of measuring triple coincidences between the satellite and hypersatellite x rays produced in filling the double vacancy, and the subsequent normal x ray accompanying the K-shell internal conversion of the 35-keV level in ^{125}Te. The coincidences were measured using two detectors; we looked for the sum of two of the x rays in one detector in coincidence with the third x ray in the other detector.

A 100 nCi source was prepared by evaporating several drops of an active solution of carrier-free NaI in 1.0 N NaOH onto cellophane tape, and sealing the dried tape with a similar piece. The source was sandwiched between

two intrinsic Ge detectors placed face to face. One of the detectors was coaxial and had a 44-mm diameter, 49-mm depth, and a 0.5-mm-thick Be window; the other detector was planar with a 16-mm diameter, 10-mm depth, and a 0.128-mm-thick Be window. The Be windows were thick enough to stop Auger and conversion electrons associated with ^{125}I decay. The energy resolution at the Te $K\alpha$ line ($\approx$ 28 keV) was 650 eV for the coaxial detector and 300 eV for the planar detector.

The detectors were connected to amplifiers equipped with pileup rejection circuitry. A standard circuit was used to generate coincidence signals. The energy and fast timing signals from each detector were digitized in two analog-to-digital converters (ADC's) and an eight-channel time-to-digital converter (TDC) in a CAMAC crate interfaced to a VAX 11/725 computer. The digitized signals were recorded event by event on magnetic tape for later analysis. To reduce the number of accumulated tapes, singles events were prescaled by factors of 800 and 400 for the coaxial and planar detectors, respectively, and $K\alpha \otimes K\alpha$ coincidences were not written to tape. The total counting time was approximately 120 days.

III. DATA ANALYSIS AND RESULTS

The magnetic tapes were replayed to generate for each detector a singles spectrum and three coincidence spectra, the first gated by $K\alpha$, the second by $K\alpha + K\alpha$, and the third by the 35-keV γ ray. The coincidence spectra were also gated by a 180-ns wide gate set on the prompt peak recorded by the TDC. In addition, the technique detailed in Ref. [1] was used to reduce the pileup of pulses that are too close (in time) to be resolved by the pileup rejection circuitry of the amplifiers.

62 sets of spectra (one per tape), each corresponding to an average of two days of data collection, were generated first. The centroids of the energy and timing peaks in each of these spectra were scanned to ensure that there were no drifts. Then the sets were added to produce four new sets each corresponding to data accumulated over approximately one month. The spectra from each one of these sets, which we shall refer to as sets 1 through 4, in order of increasing time, were analyzed separately.

Although a statistically independent yield of $K\alpha^H$ x rays could, in principle, be extracted separately from each detector, we chose to fit only the coincidence spectra of the planar detector (generated with the gates set on the coaxial detector), because it had a much better resolution. Figure 2 shows a sample singles spectrum from the coaxial detector; the shaded areas show the peaks on which the gates were set.

Figure 3 shows the $K\alpha$ region of the coincidence spectrum gated by (a) the 35-keV γ ray, and (b) the $K\alpha + K\alpha$ peak. The yield of $K\alpha^H$ x rays detected in the planar detector in coincidence with $K\alpha^N + K\alpha^S$ summed in the coaxial detector was extracted by fitting the $K\alpha$ region shown in Fig. 3(b) with six peaks superimposed on a quadratic background. The six peaks corresponded, in order of increasing energy, to the $K\alpha_2^N$, $K\alpha_1^N$, $K\alpha_2^S$, $K\alpha_1^S$, $K\alpha_2^H$, and $K\alpha_1^H$ x-ray lines. The $K\alpha^N$ peak is

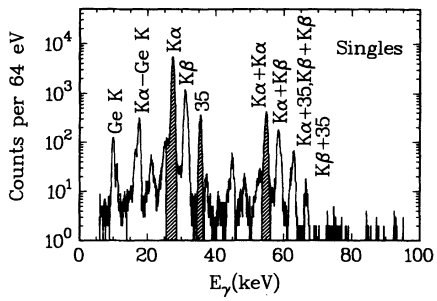

FIG. 2. A sample singles spectrum of the ^{125}I source, recorded with the coaxial detector. Coincidence spectra in the planar detector were generated by gating on the shaded peaks.

dominated by accidentals. These are of two types: (1) a true $K\alpha^N \otimes K\alpha^N$ coincidence followed by an accidental $K\alpha^N$ that sums (piles up) with the true $K\alpha^N$ to produce a pulse within the $K\alpha + K\alpha$ gate, and (2) a true $K\alpha^N + K\alpha^N$ sum in accidental coincidence with a $K\alpha^N$. There is also a much smaller number of true $K\alpha^N$ counts that arise from coincidences with the $K\alpha^S + K\alpha^H$ sum peak (the gate set on the $K\alpha + K\alpha$ sum peak in the coaxial detector was wide enough to include $K\alpha^S + K\alpha^H$ sums), and from coincidences with internal bremsstrahlung accompanying K and L capture. The $K\alpha^S$ x rays arise from true coincidences with $K\alpha^N + K\alpha^H$ sums, and the $K\alpha^H$ x rays arise from true coincidences with $K\alpha^N + K\alpha^S$ sums.

The peak shape consisted of three components: (1) a Lorentzian convoluted with a Gaussian (a Voigt profile [7, 8]), (2) an exponential tail on the low-energy side

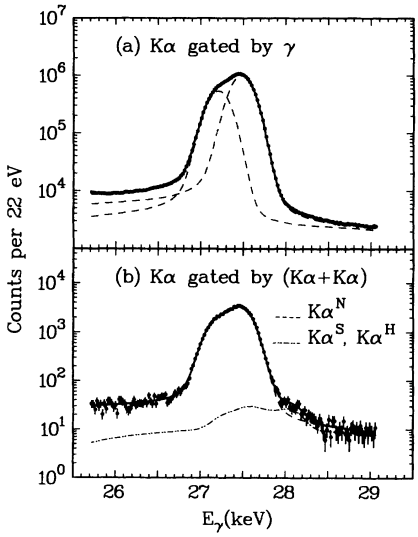

FIG. 3. (a) The $K\alpha$ region of the spectrum gated by the 35.5-keV γ ray. The dashed curves show the $K\alpha_1^N$ and $K\alpha_2^N$ components and the solid curve shows the overall fit. (b) The $K\alpha$ region of the spectrum gated by $(K\alpha + K\alpha)$. The solid curve shows the fit; the dashed curve shows the $K\alpha^N$ component of the fit while the dash-two-dotted curve shows the sum of the $K\alpha^S$ and $K\alpha^H$ components.

to account for incomplete charge collection, and (3) a step function to account for scattering of the x ray into the detector. The form of terms (2) and (3) are identical to those described in Refs. [2, 9]. The width of the Lorentzian, which is due to the short atomic lifetime of the K hole, was fixed at a value of 13 eV, obtained from the tables of Krause and Oliver [10]. The widths of the Gaussian and the exponential tail, as well as the fractional heights of the exponential tail and the step function, were fixed to values extracted from fits to the $K\alpha^N$ peak gated by the 35-keV γ ray [Fig. 3(a)]. As Fig. 3(a) shows, the assumed peak shape provides a very good fit to the data. The chi square per degree of freedom (χ^2) for fits to the $\gamma_{35} \otimes K\alpha^N$ peak was 2.54, 1.64, 1.73, and 1.78, for sets 1 through 4, respectively. Considering the very high statistical accuracy of the data ($\sim 5 \times 10^6$ counts), these χ^2 values are quite acceptable.

The ratio of the $K\alpha_1^N$ to $K\alpha_2^N$ lines was fixed to the value obtained from the fits to the $\gamma_{35} \otimes K\alpha^N$ peak. This value (1.861 ± 0.003) agrees very well with the value of 1.86, given in Ref. [6]. The ratio of the $K\alpha_1^S$ to $K\alpha_2^S$ lines was fixed to the above value, as well; however, Åberg *et al.* [11] have pointed out that this ratio decreases for $K\alpha^H$ x rays. In the fit we fixed the ratio of the $K\alpha_1^H$ to $K\alpha_2^H$ lines to 1.47, a value which we interpolated from the theoretical calculations of Chen, Crasemann, and Mark [12].

The centroids of the $K\alpha_1^N$ and $K\alpha_2^N$ lines were fixed to the values obtained from the fit to the $\gamma_{35} \otimes K\alpha^N$ peak. The centroids of the $K\alpha_1^S$ and $K\alpha_2^S$ lines were shifted from those of the corresponding $K\alpha^N$ lines by 79 eV, a value obtained from the calculations of Ref. [13]. We obtained experimental values for the energy shift of the hypersatellite lines [$\Delta K\alpha^H \equiv E(K\alpha^H) - E(K\alpha^N)$] from our fits, with the assumption that the $K\alpha_1^H$ and $K\alpha_2^H$ lines have the same shift. The shifts obtained for each of the sets are shown in Table I. The weighted average, 598 ± 26 eV, is in good agreement with the values $\Delta K\alpha_1^H = 610$ eV and $\Delta K\alpha_2^H = 607$ eV, calculated by Chen, Crasemann, and Mark [12]. In extracting the final yields of the $K\alpha^H$ x rays, the centroids of the $K\alpha_1^H$ and $K\alpha_2^H$ lines used in the fit were shifted by the above average value for all the sets. The systematic uncertainty in these extracted yields due to a ± 30 eV uncertainty in the position of the hypersatellite peak is 3%.

The small shift of the $K\alpha^S$ lines (relative to the $K\alpha^N$ lines) and the much larger yield of the $K\alpha^N$ peak [Fig. 3(b)] made the extraction of an independent value for the yield of $K\alpha^S$ x rays very difficult. Indeed, the purpose of including the $K\alpha^S$ peaks in the fit to the $K\alpha$ region gated by $K\alpha + K\alpha$ was not to get an independent yield of $K\alpha^S$, but rather to make sure that the shape of the fitting function was as accurate as possible. Since the gate on the coaxial detector was wide enough to include $K\alpha^N + K\alpha^H$ sums, the yield of $K\alpha^S$ x rays should, on average, be the same as the yield of $K\alpha^H$ x rays. Accordingly, in the fitting procedure the yield of $K\alpha^S$ x rays was fixed to be the same as that of $K\alpha^H$ x rays. (The difference in the efficiency of the detectors for $K\alpha^N$ and $K\alpha^H$ x rays was found to be less than 0.2% and has been ignored.) Hence the number of free parameters in the fit was five—the yield of $K\alpha^N$ x rays, the yield of $K\alpha^H$ x rays, and the three terms in the quadratic background. The resulting yield of $K\alpha^H$ x rays for each of the data sets is shown

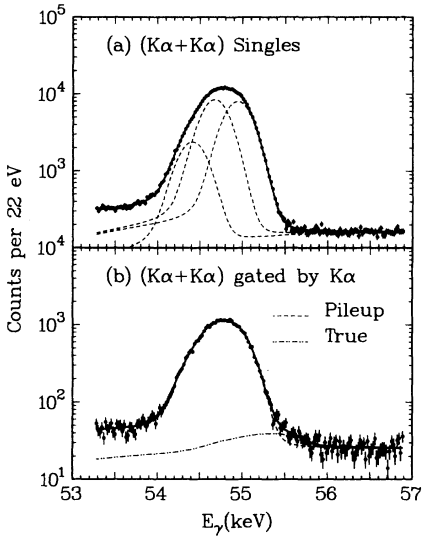

FIG. 4. (a) The $(K\alpha + K\alpha)$ region of the singles spectrum. The dashed curves show, in order of increasing energy, the $(K\alpha_2^N + K\alpha_2^N)$, $(K\alpha_1^N + K\alpha_2^N)$, and $(K\alpha_1^N + K\alpha_1^N)$ components and the solid curve shows the overall fit. (b) The $(K\alpha + K\alpha)$ region of the spectrum gated by $K\alpha$. The solid curve shows the fit; the dashed curve shows the pileup $(K\alpha^N + K\alpha^N)$ component of the fit while the dash-two-dotted curve shows the sum of the true $(K\alpha^i + K\alpha^j)$ components, where one of $\{i, j\}$ is a satellite or a hypersatellite.

TABLE I. Experimental results.

Set	1	2	3	4	Average
$N[(K\alpha^N)_1 \otimes (\gamma)_2]$	8.36×10^6	5.95×10^6	5.20×10^6	3.76×10^6	
$\Delta K\alpha^H$ (eV)	664 ± 60	632 ± 50	542 ± 50	576 ± 50	598 ± 26
$N[(K\alpha^H)_1 \otimes (K\alpha^N + K\alpha^S)_2]$	153 ± 35	114 ± 25	94 ± 20	57 ± 15	
$N[(K\alpha^S + K\alpha^H)_1 \otimes (K\alpha^N)_2]$	54 ± 25	58 ± 20	36 ± 16	52 ± 10	
$10^5 P_{KK}$ [a]	1.43 ± 0.33	1.50 ± 0.33	1.42 ± 0.30	1.19 ± 0.31	1.38 ± 0.16
$10^5 P_{KK}$ [b]	0.88 ± 0.42	1.33 ± 0.46	0.95 ± 0.42	1.89 ± 0.36	1.31 ± 0.21

[a] Deduced from $N[(K\alpha^H)_1 \otimes (K\alpha^N + K\alpha^S)_2]$.
[b] Deduced from $N[(K\alpha^S + K\alpha^H)_1 \otimes (K\alpha^N)_2]$.

TABLE II. Centroids and relative intensities used in the fit to the $(K\alpha + K\alpha)_1$ peak in coincidence with $(K\alpha)_2$.

Component	E (keV)	Rel. intensity
$K\alpha_2^N + K\alpha_2^N$	54.404	1.00
$K\alpha_2^N + K\alpha_1^N$	54.674	3.64
$K\alpha_1^N + K\alpha_1^N$	54.944	3.46
$K\alpha_2^N + K\alpha_2^S$	54.483	0.75
$K\alpha_2^N + K\alpha_1^S$	54.753	2.78
$K\alpha_1^N + K\alpha_1^S$	55.023	2.58
$K\alpha_2^N + K\alpha_2^H$	55.002	0.86
$K\alpha_2^N + K\alpha_1^H$	55.272	2.88
$K\alpha_1^N + K\alpha_1^H$	55.542	2.36
$K\alpha_2^S + K\alpha_2^H$	55.002	0.86
$K\alpha_2^S + K\alpha_1^H$	55.272	2.88
$K\alpha_1^S + K\alpha_1^H$	55.542	2.36

in Table I. The χ^2's for sets 1 through 4 were 0.88, 0.96, 1.00, and 1.08, respectively. Figure 3(b) shows the sum of data for the four sets and the result of a fit to this sum.

A statistically independent yield of $K\alpha^H$ x rays (detected in the planar detector) was extracted by fitting the $K\alpha + K\alpha$ region of the spectrum gated by $K\alpha$ x rays (detected in the coaxial detector). Since the $K\alpha$ gate on the coaxial detector was wide enough to include $K\alpha^S$ and $K\alpha^H$ x rays, as well as $K\alpha^N$ x rays, the $K\alpha + K\alpha$ region of the coincidence spectrum in the planar detector will include sums from $K\alpha^N + K\alpha^N$, $K\alpha^N + K\alpha^S$, $K\alpha^N + K\alpha^H$, and $K\alpha^S + K\alpha^H$, x rays. Accounting for the α_1 and α_2 components of each x ray and ignoring the small (3 eV) difference between the shifts of the $K\alpha_1^H$ and $K\alpha_2^H$ lines, one gets the 12 peaks listed in Table II. Using the fact that the yields of the satellite and hypersatellite x rays should be the same and that the relative intensities of the $K\alpha_1$ to $K\alpha_2$ lines are $(K\alpha_1/K\alpha_2)^N = (K\alpha_1/K\alpha_2)^S = 1.86$ and $(K\alpha_1/K\alpha_2)^H = 1.47$, we determined the relative intensities of the three lines involved in the (mostly accidental) $K\alpha^N + K\alpha^N$ sum and the nine lines involved in the $K\alpha^N + K\alpha^S$, $K\alpha^N + K\alpha^H$, and $K\alpha^S + K\alpha^H$ sums. These relative intensities are listed in Table II. The shape parameters used in the peak fits were fixed to values obtained from fitting the $K\alpha^N + K\alpha^N$ region in the singles spectrum (Fig. 4). Thus, although 12 lines were included in the fit to the $K\alpha + K\alpha$ coincidence peak, there were only five free parameters—the yield of $K\alpha^N$ x rays, the yield of $K\alpha^H$ x rays, and the three terms in the quadratic background. The resulting yield of $K\alpha^H$ x rays for each of the data sets is shown in Table I. The χ^2's for sets 1 through 4 were 1.12, 1.13, 0.93, and 1.00, respectively. Figure 4(b) shows the sum of data for the four sets and the results of a fit to this sum.

The number of $K\alpha^H$ x rays detected in the planar detector in coincidence with the $K\alpha^N + K\alpha^S$ sum detected in the coaxial is related to P_{KK} by

$$N[(K\alpha^H)_1 \otimes (K\alpha^N + K\alpha^S)_2] = N_0 P_K P_{KK} \left(\frac{\alpha_K}{1+\alpha}\right) \left[\omega_K^H \left(\frac{K\alpha}{K_T}\right)^H (\epsilon_{K\alpha^H})_1\right] \times \left[\omega_K^N \left(\frac{K\alpha}{K_T}\right)^N (\epsilon_{K\alpha^N})_2\right] \left[\omega_K^S \left(\frac{K\alpha}{K_T}\right)^S (\epsilon_{K\alpha^S})_2\right] \epsilon_c , \quad (1)$$

where N_0 is the number of ^{125}I EC decays, P_K the fraction of K-capture decays; α_K and α are, respectively, the K-shell and total internal conversion coefficients of the 35-keV level in ^{125}Te, and $\alpha_K/(1+\alpha)$ is the fraction of K-shell internal conversion decays of the 35-keV level; ω_K^N, ω_K^S, and ω_K^H are the fluorescence yields, respectively, for Te K^N, K^S, and K^H x rays; $(K\alpha/K_T)^N$, $(K\alpha/K_T)^S$, and $(K\alpha/K_T)^H$ are, respectively, the fractions of normal, satellite, and hypersatellite $K\alpha$ x rays; $(\epsilon_{K\alpha^H})_1$, $(\epsilon_{K\alpha^N})_2$, and $(\epsilon_{K\alpha^S})_2$ are the absolute efficiencies for detecting the respective x rays in the planar (subscript 1) and coaxial (subscript 2) detectors, and ϵ_c is the coincidence efficiency, which is the fraction of real coincidence events selected by the fast timing software gates.

The number of recorded coincidences between the 35-keV γ ray and $K\alpha^N$ x rays, $N[(K\alpha^N)_1 \otimes (\gamma)_2]$, is given by

$$N[(K\alpha^N)_1 \otimes (\gamma)_2] = N_0 P_K \left[\left(\frac{1}{1+\alpha}\right)(\epsilon_\gamma)_2\right] \left[\omega_K \left(\frac{K\alpha}{K_T}\right)^N (\epsilon_{K\alpha^N})_1\right] \epsilon_c . \quad (2)$$

One can then obtain P_{KK} by dividing Eq. (1) by Eq. (2) and rearranging. We simplify the result by noting that $\epsilon_{K\alpha^H} = \epsilon_{K\alpha^S} = \epsilon_{K\alpha}$ to better than 0.2%, and that $\omega_K^H \simeq \omega_K^S \simeq \omega_K$ [12]. Although the intensity ratio $(K\alpha_1/K\alpha_2)$ is smaller for hypersatellite x rays than for normal x rays [11], the calculations of Chen, Crasemann, and Mark [12], and the measurement of Isozumi, Briançon, and Walen [14] on ^{131}Cs show that the ratio $(K\alpha/K_T)^H$ is essentially the same as that for normal lines. Therefore we take $(K\alpha/K_T)^H = (K\alpha/K_T)^S = (K\alpha/K_T)^N$. With these simplifications P_{KK} can be obtained as

$$P_{KK} = \frac{N[(K\alpha^H)_1 \otimes (K\alpha^N + K\alpha^S)_2]}{N[(K\alpha^N)_1 \otimes (\gamma)_2]} \frac{1}{[\omega_K (K\alpha/K_T)]^2} \frac{1}{\alpha_K} \frac{(\epsilon_\gamma)_2}{[(\epsilon_{K\alpha})_2]^2} . \quad (3)$$

A similar expression relates P_{KK} to the $(K\alpha^S + K\alpha^H)_1 \otimes (K\alpha^N)_2$ coincidence yield.

We note here that the internal conversion coefficient depends on the number of electrons in the K shell and, in principle, the α appearing in Eq. (1) should be different from that appearing in Eq. (2). However, the atomic half-lives of the single and double holes in the K shell are on the order of 10^{-16} s [12], which is much shorter than the 1.48-ns half-life of the 35-keV level [5]. Hence the holes are nearly always filled by the time the 35-keV level decays, and α is essentially the same for double and triple coincidences.

The absolute efficiency of each detector was determined from the singles spectra by comparing the yield of the $K\alpha + K\alpha$ sum peak to the total $K\alpha$ yield: The total (i.e., photopeak plus everything summing with the photopeak) yield of $K\alpha$ x rays is given by

$$N(K\alpha) = N_0 \omega_K \left(\frac{K\alpha}{K_T}\right)\left(P_K + \frac{\alpha_K}{1+\alpha}\right)\epsilon_{K\alpha}, \quad (4)$$

while the number of $K\alpha + K\alpha$ sum coincidences is given by

$$N(K\alpha + K\alpha) = N_0 \left[\omega_K \left(\frac{K\alpha}{K_T}\right)\right]^2 \left(P_K \frac{\alpha_K}{1+\alpha}\right)\epsilon_{K\alpha}^2. \quad (5)$$

Dividing Eq. (5) by Eq. (4) and rearranging one gets the efficiency:

$$\epsilon_{K\alpha} = \frac{N(K\alpha + K\alpha)}{N(K\alpha)} \frac{1}{\omega_K (K\alpha/K_T)} \left(\frac{1+\alpha}{\alpha_K} + \frac{1}{P_K}\right). \quad (6)$$

The efficiency for 35-keV γ rays can be obtained from the above efficiency and the relative yields of 35-keV γ's and $K\alpha$'s in the singles spectra (taking summing into account). The atomic variables that enter into the calculation of the efficiencies and of P_{KK} are listed in Table III. The above method of extracting the efficiencies has the following advantages over using standard calibrated sources: there are no single line (standard) sources that bracket the energy range of interest; multiple line sources, such as ^{57}Co and ^{133}Ba, for example, require nontrivial summing corrections at the small source-to-detector distances used in this study. More importantly, the above method ensures that absorption in the ^{125}I source is properly taken into account. At these low energies the absorption in the calibration sources might be substantially different, unless they are prepared identically to the ^{125}I source.

TABLE III. Parameters relevant to the calculation of efficiencies and of P_{KK}.

ω_K [a]	0.875
(K_α/K_T) [a]	0.816
P_K [b]	0.797
α_K [b]	11.986
α [b]	14.02
$(\epsilon_{K\alpha})_1$	0.131
$(\epsilon_{K\alpha})_2$	0.229
$(\epsilon_\gamma)_2$	0.250

[a] Reference [6].
[b] Reference [5].

The values of P_{KK} extracted from the $(K\alpha^H)_1 \otimes (K\alpha^N + K\alpha^S)_2$ and $(K\alpha^S + K\alpha^H)_1 \otimes (K\alpha^N)_2$ coincidence yields are listed in Table I for each of the four data sets. The agreement of the P_{KK}'s over the four sets assures us of the following: (1) The peak shape used in the fitting procedure separates the contribution of the $K\alpha^N$ tail to the $K\alpha^H$ peak properly. Since the very large $K\alpha^N$ peak [Fig. 3(b)] is dominated by accidentals, its area relative to the small $K\alpha^H$ peak decreased appreciably over the four sets (collected over two source half-lives). (2) The $K\alpha^H$ peak is indeed associated with ^{125}I, since the source strength decreased by a factor of 4 over the measuring period, but the value of P_{KK} (which, of course, should be independent of source strength), remained the same. If the hypersatellite peak were due to a contaminant, or were spurious, the extracted value of P_{KK} would have changed over time (unless, of course, a contaminant not only produced a peak at the expected position of the hypersatellite peak, but also had a half-life very similar to that of ^{125}I—a highly unlikely possibility).

We should remark here that the reason the (fractional) statistical uncertainty in the yield of $K\alpha^H$ remained approximately the same over the four sets, even though the yield had decreased over time, is that a substantial portion of the uncertainty arises from the tail of the accidental $K\alpha^N$ peak and from the background underneath the $K\alpha^H$ peak, which is also due to pileup/accidental coincidences. The contribution of these accidentals to the error decreases with decreasing source strength. Table I also shows that the yield of $(K\alpha^H)_1 \otimes (K\alpha^N + K\alpha^S)_2$ coincidences is larger than the yield of $(K\alpha^S + K\alpha^H)_1 \otimes (K\alpha^N)_2$ coincidences. This is simply because the efficiency of the planar detector is smaller than that of the coaxial detector (Table III), so that detecting two x rays in the coaxial detector and one in the planar is more efficient than detecting two in the planar and one in the coaxial.

The average value of P_{KK} extracted from the $(K\alpha^H)_1 \otimes (K\alpha^N + K\alpha^S)_2$ coincidence peak is $(1.38 \pm 0.16) \times 10^{-5}$, while the average value extracted from the $(K\alpha^S + K\alpha^H)_1 \otimes (K\alpha^N)_2$ coincidence peak is $(1.31 \pm 0.21) \times 10^{-5}$. Each of these values is the weighted average over the four sets. Because the $K\alpha^H$ peak appears in a different region of the spectrum for each of the two gates, the agreement between these two values of P_{KK} shows that it is highly unlikely that the $K\alpha^H$ peaks are due to contaminants.

The statistically weighted average of the two values of P_{KK} is $(1.35 \pm 0.13) \times 10^{-5}$. We estimate that the overall systematic uncertainty, due to the efficiency determination, the fitting procedure, and the various other approximations we made, is less than 6%. We combine this systematic error in quadrature with the statistical error and report a final value of $P_{KK} = (1.35 \pm 0.15) \times 10^{-5}$

IV. DISCUSSION

In Table IV we compare our result for ^{125}I, as well as those for the other 14 isotopes for which measurements of P_{KK} have been made, with the theoretical predictions of Intemann's SRP calculations [3] and Suzuki and Law's SCF method [4]. The experimental values have been mostly drawn from Isozumi's recent summary of high-resolution data [15]. We also list in Table IV Q_0, the energy released in each decay, and, to quantify how close this energy is to the K-shell binding energy, we also tabulate the quantity

$$\left(\frac{Q_2}{Q_1}\right)^2 \equiv \left(\frac{Q_0 - B_L}{Q_0 - B_K}\right)^2, \tag{7}$$

where B_K and B_L are the K-shell and L_1-shell binding energies, respectively. Obviously, this quantity will be larger the closer the decay energy is to threshold, with its value ranging from $\gtrsim 1$ for decays far from threshold ($Q_0 \gg B_K$), to $\lesssim 4$ for decays close to the double K-shell ionization threshold ($Q_0 = 2B_K$). The reason we chose this quantity to characterize how close a decay is to threshold will be stated shortly.

Table IV shows that, generally speaking, P_{KK} decreases with increasing Z. The nuclides with low Q_0 values, namely, ^{109}Cd, ^{125}I, ^{139}Ce, and ^{181}W, have P_{KK}'s that are lower than the general trend, with the P_{KK} value being smaller the lower the Q_0. The theoretical predictions bracket most of the measured values, with the SCF theory being on the high side and the SRP theory on the low side. For decays with low Q_0, both theories predict P_{KK}'s that are lower than the average trend, as well; however, both theoretical predictions fall to zero (with decreasing Q_0) faster than the experimental values. This point is illustrated in Fig. 5, which shows the ratio of the experimental to theoretical P_{KK}'s, and $(Q_2/Q_1)^2$ for each decay. The ratio for decays with large values of $(Q_2/Q_1)^2$ (i.e., low Q_0) is larger than the average trend in both theories.

P_{KK} depends on the Q value through the phase-space dependence of the ejected electron on the Q value; this

TABLE IV. Comparison of various theories with recent experimental results.

Nuclide	Q_0 [a] (keV)	B_K [a] (keV)	B_L [a] (keV)	$(Q_2/Q_1)^2$	$10^5 P_{KK}$ I [b]	SL [c]	Empir. [d]	Expt. [e]
^{37}Ar	813.8	2.8	0.3	1.01	25.84	52.94	16.18	37±9 [f]
^{54}Mn	542.2	6.0	0.7	1.02	11.25	24.3	8.05	36±3
^{55}Fe	231.4	6.5	0.8	1.05	9.42	20.1	7.27	12.8±1.8 [g]
^{65}Zn	1351.9	9.0	1.1	1.01		15.3	5.54	22±2
^{71}Ge	235.7	10.4	1.3	1.08	5.08	11.84	4.64	12 [h]
^{85}Sr	550.0	15.2	2.1	1.05	3.38	9.38	3.32	6.0±0.5
^{103}Pd	506.3	23.2	3.4	1.08	1.74	6.03	2.20	3.13±0.31
^{109}Cd	94.3	25.5	3.8	1.73	0.34	0.89	1.17	1.02±0.36
^{113}Sn	647.1	27.9	4.2	1.08	1.34	5.33	1.86	1.5±0.5 [i]
^{125}I	150.6 [j]	31.8	4.9	1.50	0.425 [k]	0.95 [l]	1.20	1.35±0.15 [m]
^{131}Cs	347.0 [n]	36.0	5.5	1.21	0.75	3.22	1.40	1.4±0.1
^{139}Ce	99.0	38.9	6.3	2.38	0.026 [k]	0.084 [l]	0.22	0.20±0.16 [o]
^{165}Er	377.1	55.6	9.4	1.31	0.26	1.71	0.85	0.77±0.23 [p]
^{181}W	188.0	67.4	11.7	2.14	0.022	0.14	0.26	0.24±0.06
^{207}Bi	771.7	88.0	16.4	1.22	0.11	1.97	0.48 [q]	0.6±0.25

[a] Reference [6], unless otherwise noted.
[b] I: Intemann's SRP theory [3].
[c] SL: Suzuki and Law's SCF theory [4], using the local density approximation.
[d] Empir: Empirical calculation using Eq. (13).
[e] Experimental values are from Isozumi's review [15], unless otherwise noted.
[f] Reference [16].
[g] Weighted average of $(12 \pm 4) \times 10^{-5}$ [17] and $(13 \pm 2) \times 10^{-5}$ [2].
[h] Reference [18].
[i] Reference [19].
[j] Reference [20].
[k] Reference [21].
[l] Reference [22].
[m] Present work.
[n] Reference [23].
[o] Reference [1].
[p] Weighted average of values given in Ref. [15].
[q] Calculated using $(Q_2/Q_1)^4$ instead of $(Q_2/Q_1)^2$ in Eq. (13). See also [28].

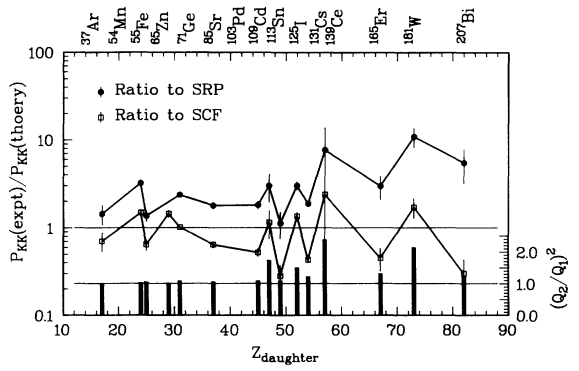

FIG. 5. Ratios of the experimental values of P_{KK} to the theoretical values of Intemann (solid circles) and of Suzuki and Law (open squares). The values are plotted at the Z of the daughter atom. The solid bars show $(Q_2/Q_1)^2$ for each of the decays (scale shown on the right axis).

dependence is modified from that of a simple plane wave due to the Coulomb interaction of the ejected electron with the daughter atom. It might seem that there is no simple way of exhibiting this dependence analytically, especially for decays with low Q value, where the ejected electron's wave function depends sensitively on the screening of the nuclear potential by the atomic electrons. There is, however, a simple (albeit approximate) way of explicitly exhibiting the dependence of P_{KK} on the decay energy. This involves relating P_{KK} to the probability $P^{(0)}$ of leaving zero holes in the K shell per K capture. (Zero holes can be obtained via the shakedown of higher orbit electrons to the K shell, during electron capture.) The connection between P_{KK} and $P^{(0)}$ is [24, 25]

$$P_{KK} \equiv P^{(2)} = 1 - P^{(1)} - P^{(0)}, \tag{8}$$

where $P^{(1)}$ is the probability, per K capture, of leaving one hole in the K shell. Using a notation similar to that of Mukoyama *et al.* [26], $P^{(1)}$ and $P^{(0)}$ are given by

$$P^{(1)} = |\langle\psi_f(Z',K)|\psi_i(Z,K)\rangle|^2, \tag{9}$$

$$P^{(0)} = \sum_{n=2}^{n'} (Q_n/Q_1)^2 |\langle\psi_f(Z',K)|\psi_i(Z,n)\rangle|^2, \tag{10}$$

where $\langle\psi_f(Z',K)|\psi_i(Z,n)\rangle$ is the atomic-wave-function overlap of the ns state of the parent atom with the $1s$ state of the daughter atom; $Q_1 = Q_0 - B_K$ is the energy released in K capture [27], and $Q_n = Q_0 - B_n$, is the energy released in K capture accompanied by shakedown from the ns shell, B_n being the binding energy of an electron in the ns state of the daughter atom [28]. Following our earlier work [1], we make the reasonable approximation

$$\begin{aligned} P^{(0)} &\simeq (Q_2/Q_1)^2 \sum_{n=2}^{n'} |\langle\psi_f(Z',K)|\psi_i(Z,n)\rangle|^2 \\ &\equiv (Q_2/Q_1)^2 M^{SD}, \end{aligned} \tag{11}$$

where, as in [1], M^{SD} is introduced as a shorthand for the sum over the squares of the shakedown matrix elements. With this approximation P_{KK} can be written as

$$P_{KK} = 1 - P^{(1)} - (Q_2/Q_1)^2 M^{SD}. \tag{12}$$

Equation (12) exhibits the dependence of P_{KK} on the Q value explicitly. The reason we chose the quantity $(Q_2/Q_1)^2$ to characterize how close a decay is to threshold is now clear. The sensitivity of P_{KK} to low Q values depends on the relative sizes of the quantities $(1 - P^{(1)})$ and M^{SD} and on how large $(Q_2/Q_1)^2$ is. From a comparison between the P_{KK}'s of ^{139}Ce and ^{131}Cs Hindi and Kozub [1] estimated M^{SD} for ^{131}Cs to be 1.0×10^{-5}, and hence $(1 - P^{(1)})$ to be 2.6×10^{-5}.

Using these two numbers one can estimate P_{KK} for decays with different Q values, provided the atomic number is close to that of Cs. In order to estimate P_{KK} for decays with different Z, as well as different Q value, the Z dependence of the quantities $(1 - P^{(1)})$ and M^{SD} would have to be known. In Table IV we show the values of P_{KK} calculated using the equation

$$P_{KK} = \left(\frac{54}{Z}\right)^2 [2.6 - (Q_2/Q_1)^2 1.0] \times 10^{-5}, \tag{13}$$

that is, assuming a $1/Z^2$ dependence for both $(1 - P^{(1)})$ and M^{SD}, which is the dependence predicted by the (nonrelativistic) Primakoff-Porter theory [24]. The agreement of Eq. (13) with the measured P_{KK}'s of isotopes with $Z > 40$ is quite remarkable; in particular, the agreement with the measured value for ^{181}W, which has a P_{KK} that is lower than the general trend by about a factor of 3, shows that this equation does a reasonable job of predicting the Q dependence of P_{KK}.

For $Z < 40$, the P_{KK}'s predicted by Eq. (13) are lower than the measured values by a factor of ≈ 2, suggesting a dependence stronger than $1/Z^2$ and/or different dependencies for $(1 - P^{(1)})$ and M^{SD}. One obvious factor which Eq. (13) does not take into account is the change in the number of matrix elements contributing to M^{SD} in Eq. (11). For lower Z's there will be a fewer number of electrons that can contribute to the shakedown matrix elements and hence M^{SD} will not increase as much as expected from the simple $1/Z^2$ dependence of the matrix elements. If this factor were taken into account, the P_{KK}'s predicted by Eq. (13) would be slightly higher at lower Z, bringing them into closer agreement with the measured values.

Our aim here was not to provide quantitative predictions for P_{KK}, but rather to see if one can use the measured values for some of the isotopes to estimate P_{KK} for other isotopes, in a way that takes into account not only the general decrease of P_{KK} with higher Z, but also deviations from the smooth general decrease for decays with low Q value. The agreement of Eq. (13) with the measured values for several isotopes suggests that such estimates are possible. A more general approach would be to parametrize $(1 - P^{(1)})$ and M^{SD} as functions of Z and to determine the parameters from a global fit to the available data. Obviously, it would be desirable to have

a larger sample of accurately measured P_{KK}'s, especially for isotopes with low Q values, before such an approach is taken.

To summarize, we have determined P_{KK} for the EC decay of ^{125}I to be $(1.35 \pm 0.15) \times 10^{-5}$. This value confirms that the theories of Suzuki and Law [4], and of Intemann [3], which bracket most of the existing measurements, consistently underestimate P_{KK} for decays with low Q values.

ACKNOWLEDGMENTS

We wish to thank Professor Robert Intemann, Professor Akira Suzuki, and Professor James Law for providing us with the theoretical predictions of P_{KK} for ^{125}I. The assistance of James Parker in collecting the data is gratefully acknowledged. This work was supported by the U.S. Department of Energy, Nuclear Physics Division, via Grant No. DE-FG05-87ER40314.

[1] M.M. Hindi and R.L. Kozub, Phys. Rev. C **43**, 461 (1991), and references therein.
[2] J.L. Campbell, J.A. Maxwell, and W.J. Teesdale, Phys. Rev. C **43**, 1656 (1991); see, however, M.M. Hindi, R.L. Kozub, H.J. Nagy, and G. Schupp, *ibid.* **44**, 2237 (1991).
[3] R.L. Intemann, Phys. Rev. C **31**, 1961 (1985).
[4] A. Suzuki and J. Law, Phys. Rev. C **25**, 514 (1982).
[5] T. Tamura, Z. Matumoto, and M. Ohshima, Nucl. Data Sheets **32**, 497 (1981).
[6] *Table of Isotopes*, 7th ed., edited by C.M. Lederer and Virginia S. Shirley (Wiley, New York, 1978).
[7] R. Gunnink, Nucl. Instrum. Methods **143**, 145 (1977).
[8] M. Mori, Publ. Res. Inst. Math. Sci. **19**, 1081 (1983).
[9] David Radford, Internal Report No. 98, WNSL, Yale University, 1979 (unpublished).
[10] M.O. Krause and J.J. Oliver, J. Phys. Chem. Ref. Data **8**, 329 (1979).
[11] R. Åberg, J.P. Briand, A.P. Chevalier, A. Chetioui, J.P. Rozet, M. Tavernier, and A. Touati, J. Phys. B **9**, 2815 (1976).
[12] M.H. Chen, B. Crasemann, and H. Mark, Phys. Rev. A **25**, 391 (1982).
[13] D. Burch, L. Wilets, and W.E. Meyerhof, Phys. Rev. A **9**, 1007 (1974).
[14] Y. Isozumi, Ch. Briançon, and R.J. Walen, Phys. Rev. C **25**, 3078 (1982).
[15] Y. Isozumi, Nucl. Instrum. Methods **A280**, 151 (1989).
[16] R.W. Kiser and W.H. Johnston, J. Am. Chem. Soc. **81**, 1810 (1959).
[17] J.P. Briand, P. Chevalier, A. Johnson, J.P. Rozet, M. Tavernier, and A. Touati, Phys. Lett. **49A**, 51 (1974).
[18] J.P. Briand, P. Chevalier, M. Tavernier, and J.P. Rozet, Phys. Rev. Lett. **27**, 777 (1971).
[19] P. Venugopala Rao, I.J. Unus, P.A. Indira, Ali M. Guima, and V.R. Veluri, Proceedings of the International Conference on X-ray and Atomic Inner-Shell Physics, Eugene, Oregon, 1982 (unpublished).
[20] M.J.G. Borge, A. De Rujula, P.G. Hansen, B. Jonson, G. Nyman, H.L. Ravn, K. Riisager, and the ISOLDE Collaboration, Phys. Scr. **34**, 591 (1986).
[21] R.L. Intemann (private communication).
[22] A. Suzuki and J. Law (private communication).
[23] A.H. Wapstra and G. Audi , Nucl. Phys. **A432**, 1 (1985).
[24] H. Primakoff and F.T. Porter, Phys. Rev. **89**, 930 (1953).
[25] J.S. Levinger, Phys. Rev. **90**, 11 (1953).
[26] T. Mukoyama, Y. Isozumi, T. Kitahara, and S. Shimizu, Phys. Rev. C **8**, 1308 (1973).
[27] We use a notation that is slightly different from that used in Ref. [1]: Q_1 here denotes the quantity that was denoted by Q_0 in Ref. [1].
[28] The Q dependence in Eq. (10) holds for allowed and first forbidden nonunique decays, which is the case for all isotopes listed in Table IV except ^{207}Bi. For unique first forbidden decays, such as the dominant $\frac{9}{2}^- \rightarrow \frac{13}{2}^+$ transition in ^{207}Bi, the term $(Q_n/Q_1)^2$ in Eq. (10) becomes $(Q_n/Q_1)^4$.